Development of Coupled Particle Hypersonic Flowfield-Photon Monte Carlo Radiation Methods

T. Ozawa,* D. A. Levin,† A. Wang,‡ and M. Modest§
Pennsylvania State University, University Park, Pennsylvania 16802

With its fast reentry speed, the Stardust vehicle generated a strong shock region ahead of its blunt body with a translational temperature in excess of 60,000 K. Such an extreme Mach number flow is sufficiently energetic to initiate gas ionization processes and thermal and chemical ablation processes. The generated charged species affect nonequilibrium atomic and molecular energy distributions and shock layer radiation. In this work, we present the first loosely coupled direct simulation Monte Carlo simulations with the particle-based photon Monte Carlo method to simulate high-Mach-number reentry flows in the near-continuum to transitional flow regimes. Eleven species including five ionization processes were modeled in direct simulation Monte Carlo, and the average ion velocity model was used to simulate the electron motion. The degree of ionization is predicted to be between 3–7% along the stagnation line for altitudes of 68.9 and 81 km, and the maximum translational and electron temperatures are approximately 60,000 and 20,000 K, respectively. To efficiently capture the nonequilibrium radiation generated by this flow, emission and absorption coefficient databases using the Nonequilibrium Air Radiation computational tool were generated. However, in contrast to the Nonequilibrium Air Radiation computational tool, radiative transport was modeled by the particle-based photon Monte Carlo method instead of the simplified one-dimensional tangent-slab approximation. It was found that the atomic nitrogen emission is approximately 1 order of magnitude higher than the atomic oxygen emission along the stagnation line due to the higher concentration of atomic nitrogen at this altitude. The radiation energy change calculated by the particle-based photon Monte Carlo method was coupled with the direct simulation Monte Carlo calculations, and it was found that although the atomic nitrogen and atomic oxygen atomic radiation does not have an important impact on the flowfield at 81 km, the stronger radiation modified the flowfield and heat flux at the wall at an altitude close to peak heating.

Nomenclature

b_{hw}	=	half width of the line broadening, Å
E_{abs}	=	integrated absorption energy, W/cm³
$E_{abs,p}$	=	absorption energy per particle, W
E_{emis}	=	integrated emission energy, W/cm³
$E_{emis,p}$	=	emission energy per particle, W
E_{ray}	=	energy of a ray, photon bundle, W
F_{num}	=	Number of particles represented by a simulated particle
i	=	cell index in the x direction
j	=	cell index in the r direction
k	=	line index
$k_{1,db}(\lambda)$	=	number of lines for $\lambda_i < \lambda - b_{hw,max}$ in the database
$k_{2,db}(\lambda)$	=	number of lines for $\lambda_i < \lambda + b_{hw,max}$ in the database
N_c	=	number of particles in a cell
N_y	=	umber of cells in the r direction
n_a	=	atom number density, cm⁻³
n_e	=	electron number density, cm⁻³
n^+	=	ion number density, cm⁻³
Q_{emis}	=	integrated emission coefficient, W/cm³/sr
$Q_{emis,k}$	=	accumulated atomic emission lines from $i = 1$ to k in order of increasing wavelength, W/cm³/sr
$Q_{emis,\lambda}$	=	partially integrated emission coefficient, W/cm³/sr
R_λ	=	uniform random number between 0 and 1
r	=	radial coordinate, same as y
r_{cn}	=	local cone radius of a ray, cm
T_e	=	electron temperature, K
T_{rot}	=	rotational temperature, K
T_{tr}	=	translational temperature, K
T_{vib}	=	vibrational temperature, K
V_c	=	volume of a cell, cm³
W_{2D}	=	spatial weighting function in 2-D
x	=	coordinate in the flow direction
ε_i	=	emission line strength of a bound–bound transition at the centerline, W/cm³/sr
$\nabla \cdot q$	=	radiative energy change, $= E_{emis} - E_{abs}$
$\nabla \cdot q_R$	=	radiative heat flux in W/cm²
$\Delta\tau$	=	contribution of a specific particle to the optical thickness, dimensionless
ε_λ	=	emission coefficient at a wavelength λ, W/cm³/sr/Å
κ_λ	=	absorption coefficient, cm⁻¹
λ	=	wavelength, Å
λ_i	=	wavelength of a bound–bound transition centerline, Å
$\sigma_{abs,\lambda}$	=	absorption cross section, cm² $(= \kappa_\lambda / n_a)$
τ	=	optical thickness, dimensionless
ϕ	=	line broadening function

Subscripts

c	=	cell
cn	=	cone
D	=	doppler
db	=	database
e	=	electron
p	=	particle

*Project Researcher, Department of Aerospace Engineering, 233 Hammond Building; Aerospace Research and Development Directorate, Japan Aerospace Exploration Agency, 7-44-1 Jindaiji Higashi, Chofu, Tokyo 182-8522, Japan; ozawa.takashi@jaxa.jp. Member AIAA.
†Professor, Department of Aerospace Engineering, 233 Hammond Building; dalevin@psu.edu. Associate Fellow AIAA.
‡Department of Mechanical Engineering, 301B Reber Building; aqwang@psu.edu.
§Shaffer and George Professor of Engineering, Department of Mechanical Engineering, 392 Science & Engineering Building, University of California, Merced, CA; mmodest@eng.ucmerced.edu.

ray	=	ray
rot	=	rotational
tr	=	translational
vib	=	vibrational
λ	=	wavelength

Superscripts

bf	=	bound–free
*	=	normalized quantity
+	=	ion

I. Introduction

FOR high-speed reentry conditions, such as Stardust [1–3] or the Crew Exploration Vehicle [4–7], the radiative heat flux [8] is significant and must be accounted for in heat shield design [9]. With the fast reentry speeds (e.g., 7–12 km/s), an aeroshell vehicle can generate a strong shock region ahead of its blunt body with temperature above 60,000 K. The energetics of the reentry are sufficiently high to initiate gas ionization processes [10] and thermal and chemical ablation processes [11,12]. The generated ions and electrons lead to complicated reactions among charged and neutral particles, which further affect nonequilibrium atomic and molecular energy distributions and radiation behavior. The ratio of radiative to convective heat flux for the Stardust reentry flows was found to be high for altitudes lower than 80 km, and thus coupling between flowfield and radiation calculations may be required.

In terms of previous research, Olynick et al. [1] applied a continuum Navier–Stokes flow solver loosely coupled to radiation and material thermal ablation models to predict the Stardust reentry flows at altitudes of 43–80 km. Park [2] recently applied the viscous shock layer method to predict heat transfer rates for the Stardust at altitudes of 46–76 km. However, for high altitudes higher than 60 km, continuum breakdown occurs and nonequilibrium effects need to be considered. Thus, continuum methods may not be applicable for prediction of these flowfields or the derived convective and radiative heat fluxes. Gallis and Harvey [13,14] modeled nonequilibrium thermal radiation in direct simulation Monte Carlo (DSMC) as well as electronic excitation processes and obtained good agreement for the spectral intensity measurements of an air shock-tube experiment. However, for their method, accurate cross sections for electronic excitation and absorption are needed, and the cross sections are not well known for all required species. Also, even if all the cross sections were available, their implementation in a DSMC calculation would be difficult. In their work the absorption of emitted radiation was assumed to be localized in a cell, and a single absorption cross section was used for all wavelengths. The spectral radiation and the radiative transport was therefore approximate in nature.

In our previous work [10], ionization processes and charged species were modeled in the direct simulation Monte Carlo (DSMC) method. The effect of energy exchange relaxation models, chemical reactions, and charged species were discussed for the Stardust reentry body shape for altitudes spanning the transitional to the near-continuum flight regime (100 to 68.9 km). In addition, the impact of thermal and chemical ablation processes of the Stardust thermal protection layer that were designed to reduce aerodynamic heating during the entry process on the flowfield was investigated in DSMC [12]. In this work, we further develop our DSMC flowfield calculations to study the impact on the flow by loosely coupled radiation with the particle-based photon Monte Carlo (p-PMC) method [15]. In the p-PMC method, the absorption coefficient is calculated using a line–by–line database, and the emitted photons travel as far as possible until the photon bundle energy is completely absorbed by atomic oxygen (O) or atomic nitrogen (N) atoms. The advantage of the coupling between the DSMC and the p-PMC is that both are particle methods, thereby facilitating the transference of DSMC particle properties to the PMC radiative transport calculations. To use the DSMC particle information to calculate radiation on a particle basis, excitation and relaxation of electronically excited state populations needs to be modeled in DSMC. In addition, flowfield and radiation simulations need to be tightly coupled to represent different particle conditions for each time step. Currently, tightly coupled computations between DSMC and p-PMC are too expensive to be executed, and the complexity of including electronically excited states is just being under taken. Thus, in this work, a loosely coupled procedure is implemented between the DSMC and p-PMC methods [16]. Using the DSMC steady state solution (e.g., number densities, temperatures), the electronic excited states are calculated by the quasi steady state (QSS) model [17], and emission and absorption coefficients are calculated based on the electronic excited state populations. We apply the p-PMC model to simulate the radiation of Stardust hypersonic reentry flows for transitional to near-continuum conditions.

II. Modeling of Radiation

The p-PMC methods were initially developed to provide accurate modeling of the radiative source terms in turbulent combustion problems [15]. In the PMC method, the radiative transfer equation (RTE) is solved by tracing statistical photon bundles. This implies that the total energy carried by all emitted photon bundles must be equal to the PMC particle energy in the p-PMC method. So-called random number relations must be developed to obtain statistically meaningful directions and wavelengths of emitted bundles, as explained in detail in Modest [18]. In the p-PMC method, radiation transfer is modeled by allowing each particle to emit its emissive energy in the form of photon bundles (rays) into random directions. While directions of photon emission are straightforward, emission wavelengths for a nonequilibrium gas mixture require special attention. Following Modest [18]

$$R_\lambda = \frac{Q_{\text{emis},\lambda}}{Q_{\text{emis}}} = \frac{\int_{\lambda_{\min}}^{\lambda} \varepsilon_\lambda \, d\lambda}{\int_{\lambda_{\min}}^{\lambda_{\max}} \varepsilon_\lambda \, d\lambda} \tag{1}$$

where λ is the corresponding wavelength of the photon bundle emitted from a p-PMC particle. A bisection method is used to select the wavelengths of photon bundles. Once a wavelength is selected using the emission random number databases (ERND), the absorption cross section at a given wavelength $\sigma_{\text{abs},\lambda}(T_e, n_e, n^+/n_a, T_{\text{tr}})$ is calculated from the Nonequilibrium Air Radiation (NEQAIR) [19] based database [20] on the fly. The rays are traced until the ray's energy is depleted due to absorption by other particles or it escapes from the enclosure. Special schemes have been developed to simulate the ray-particle interaction and to minimize statistical errors [15]. A line–by–line spectral Monte Carlo method was also developed using random number relationships to treat the spectral variation of radiation exactly in the PMC simulations [15].

In this work, a cone-ray model is used in conjunction with a point-particle model [15]. The DSMC particle information (e.g., position, velocity, energy, temperatures, number densities, and F_{num}) is transferred to the p-PMC calculation, and the radiative energy change per particle due to emission and absorption is calculated. In the 2-D axisymmetric DSMC calculations, since radial weights are used, the F_{num} of each particle is based on its y coordinate ($j = 1, N_y$),

$$F_{\text{num}}(j) = F_{\text{num},\infty} \times (2j - 1)/(2N_y - 1) \tag{2}$$

where $F_{\text{num},\infty}$ is a number of atoms or molecules represented by a DSMC simulation particle.

Absorption and emission coefficient databases were created using the Nonequilibrium Air Radiation (NEQAIR) [19] model for use in the PMC simulation to avoid time consuming repetition of calculating these quantities. Since the NEQAIR code was developed for conditions that occur in nonequilibrium flows, our database is accurate for the existing nonequilibrium conditions. In the atomic species database the excitation population was calculated using the QSS model as a function of electron temperature T_e, electron number density n_e, and the ratio of ion to neutral number density n^+/n_a, since the electronic excited state population is linearly proportional to the ratio of n^+/n_a. Atomic lines for N and O, the major radiating species, were also databased, and emission and absorption coefficients are

databased as a function of T_e, n_e, n^+/n_a, and translational temperature T_{tr}. The translational temperature is used to simulate Doppler line broadening in this paper for each atomic line. Further details about the database can be found in the recent work of Sohn et al. [20] and Ozawa et al. [21]

The emission energy per PMC particle is calculated as

$$E_{\mathrm{emis},p} = 4\pi \int_{\lambda_{\min}}^{\lambda_{\max}} \varepsilon_\lambda^* \, d\lambda \times F_{\mathrm{num}} \qquad (3)$$

where F_{num} is the number of real molecules represented by a simulated particle. The superscript $*$ denotes a normalized quantity (i.e., divided by n_a), and ε_λ^* is the normalized emission coefficient ($\varepsilon_\lambda^* = \varepsilon_\lambda/n_a$) at a wavelength λ. The absorption energy removed from a ray by particle absorption is evaluated as

$$E_{\mathrm{abs},p} = E_{\mathrm{ray}}[1 - \exp(-\Delta\tau)] \qquad (4)$$

where $\Delta\tau$ is the contribution of a specific PMC particle to the optical thickness and E_{ray} is the ray's energy. In the p-PMC calculations $\Delta\tau$ is calculated as

$$\Delta\tau = \sigma_{\mathrm{abs},\lambda} F_{\mathrm{num}} \frac{W_{2D}(r/r_{\mathrm{cn}})}{\pi r_{\mathrm{cn}}^2} \qquad (5)$$

where r_{cn} is the local cone radius of the ray, r is a radius between the cone center to a particle, $\sigma_{\mathrm{abs},\lambda}$ is the absorption cross section, and W_{2D} is a spatial weighting function [15]. In this work, a Gaussian weight function is used, and the absorption cross section $\sigma_{\mathrm{abs},\lambda}$ is calculated as $\sigma_{\mathrm{abs},\lambda} = \kappa_\lambda/n_a$. The total optical thickness τ of the ray is the summation of $\Delta\tau$ over all ray-particle absorption events. In this work, a cold Stardust body wall is used in the p-PMC calculations, and the ray's energy is absorbed by the body if it impacts the Stardust body.

The use of ERNDs reduces the computational cost and improves the computational efficiency in the wavelength selection for the ray-tracing scheme [16]. The ERND have been developed for conditions that occur in nonequilibrium flows based on our NEQAIR-based emission and absorption coefficient database [20]. The absorption cross section $\sigma_{\mathrm{abs},\lambda}$ in each cell is also calculated by the line–by–line NEQAIR-based database. In the ERND bound–bound (bb) transitions were separated from bound–free (bf) and free–free (ff) transitions. For bb transitions, the partially integrated emission is calculated as

$$
\begin{aligned}
Q_{\mathrm{emis},\lambda}^* &= \int_{\lambda_{\min}}^{\lambda} \varepsilon_\lambda^*(T_e, n_e, n^+/n_a, T_{tr})\, d\lambda \\
&= \sum_{i \leq k_1} \varepsilon_i^*(T_e, n_e, n^+/n_a) \\
&\quad + \sum_{k_1 < i \leq k_2} \int_{\lambda - b_{\mathrm{hw,max}}}^{\lambda} \varepsilon_{\lambda,i}^*(T_e, n_e, n^+/n_a, T_{tr})\, d\lambda \\
&= Q_{\mathrm{emis},k_1}^*(T_e, n_e, n^+/n_a) + \sum_{k_1 < i \leq k_2} \varepsilon_i^* \int_{\lambda - b_{\mathrm{hw,max}}}^{\lambda} \phi_i(\lambda)\, d\lambda \qquad (6)
\end{aligned}
$$

where $\phi(\lambda)$ is the line broadening function. For bb transitions, the centerline wavelength λ_k (Å) and accumulated normalized emission coefficient, $Q_{\mathrm{emis},k}^*(T_e, n_e, n^+/n_a)$, are stored for each line k, which is defined as

$$Q_{\mathrm{emis},k}^* = \sum_{i \leq k} \varepsilon_i^*(T_e, n_e, n^+/n_a) \qquad (7)$$

i.e., the accumulated strength of all lines with $\lambda_i < \lambda_k$. The normalized coefficient is $\varepsilon_i^*(T_e, n_e, n^+/n_a)$ in units of W/sr for an atomic line i. The 170 and 86 atomic lines listed in NEQAIR for N and O, respectively, are included in the databases and are sorted in order of increasing wavelength. Based on the conditions in hypersonic reentry flowfields, the range of T_e was 1000–28000 K with a constant increment in $T_e^{0.1}$ (70 points); n_e varies from 1×10^{13}–4×10^{16} cm^{-3} with a constant increment in $[\log(n_e)]^{0.1}$ (50 points), and two values of n^+/n_a equal to 0 and 1 were used. To avoid

extrapolation, three data points were added for both the upper and lower limits of $T_e^{0.1}$ and $[\log(n_e)]^{0.1}$. The partially integrated emission $Q_{\mathrm{emis},k}^*$ was assumed to depend linearly on the ratio of n^+/n_a as

$$Q_{\mathrm{emis},k}^* = A_k \times \frac{n^+}{n_a} + B_k \qquad (8)$$

In the ERND, A_k and B_k are stored for each atomic line at all different electron temperature and number density data points. The coefficient B_k is calculated by setting n^+/n_a to 0 and A_k is calculated by setting n^+/n_a to 1 and subtracting B_k.

To evaluate Eq. (6), first the line indices k_1 and k_2 are selected as follows: k_1 is the maximum integer with $\lambda_{k1} < \lambda - b_{\mathrm{hw,max}}$, where $b_{\mathrm{hw,max}}$ is the maximum half width of line broadening that needs to be considered (set to a constant value of 0.4 Å); k_2 is the maximum integer with $\lambda_{k2} < \lambda + b_{\mathrm{hw,max}}$. In other words, $k_1 + 1$ is the first line (in order of increasing λ), for which the ϕ_λ is not yet totally integrated, while k_2 is the last line, which is affected at all by the integration. To determine k_1 and k_2, the number of accumulated lines from $\lambda_{\min}$ to a given wavelength is stored for 800–13200 Å with a resolution of 0.1 Å. The arrays contain k_1 and k_2 as a function of λ, where $k_{1,\mathrm{db}}(\lambda)$ is the number of lines for which $\lambda_i < \lambda - b_{\mathrm{hw,max}}$ and $k_{2,\mathrm{db}}(\lambda)$ is the number of lines for which $\lambda_i < \lambda + b_{\mathrm{hw,max}}$.

For bf and ff transitions the partially integrated normalized emission, $\int_{\lambda_{\min}}^{\lambda} \varepsilon_\lambda^{\mathrm{bf},*}(T_e, n_e, n^+/n_a, T_{tr})\, d\lambda$ (W/sr) as a function of λ, was stored for each T_e, n_e, and n^+/n_a condition. For bf and ff transitions, the considered wavelength range was $\lambda = 500$–6000 Å with a resolution of $\Delta\lambda = 10$ Å. For the Stardust reentry cases considered here, 68.9 and 81 km, the contribution of the ff transitions was found to be negligible. The size of the ERND, including the accumulated emission lines for bb lines, the integrated emission for bf and ff transitions, and k_1 and k_2 information, is approximately 31 MB and 26 MB for N and O, respectively.

In the p-PMC calculations, for both bb and bf transitions, a spline interpolation scheme with the power of 0.1 for T_e and the power of 0.1 for $\log(n_e)$ is used to determine the normalized emission coefficient at a given T_e and n_e. At a given n^+/n_a, a linear dependence is used. For the spline interpolations, the interpolated results were compared with the integrated emission energy obtained by NEQAIR to determine if the databased resolution for T_e and n_e was adequate. The threshold accuracy requirement for the emission and absorption coefficients was set to 0.1%. As explained before, the line indices k_1 and k_2 are selected, and the accumulated normalized atomic line strength Q_{emis,k_1}^* from $k = 1$ to k_1 is read from the ERND, and ε_k^* is calculated as

$$\varepsilon_k^* = Q_{\mathrm{emis},k}^* - Q_{\mathrm{emis},k-1}^* \qquad (9)$$

If $\Delta\lambda(=|\lambda_k - \lambda|) < b_{\mathrm{hw,max}}$, the half width of the Doppler broadening is calculated for the line, and the Doppler broadening is applied to evaluate the partial integration. Using the error function, the partially integrated normalized emission for a line is calculated as

$$S_{\mathrm{emis},i}^* = \int_{\lambda - b_{\mathrm{hw,max}}}^{\lambda} \varepsilon_{\lambda,i}^* \, d\lambda = \frac{\varepsilon_i^*}{2}\left[1 + \mathrm{erf}\left(\frac{\Delta\lambda\sqrt{\ln(2)}}{b_{D,i}}\right)\right] \qquad (10)$$

for $\lambda \geq \lambda_i$, and

$$S_{\mathrm{emis},i}^* = \frac{\varepsilon_i^*}{2}\left[1 - \mathrm{erf}\left(\frac{\Delta\lambda\sqrt{\ln(2)}}{b_{D,i}}\right)\right] \qquad (11)$$

for $\lambda < \lambda_i$. For continuum radiation, linear interpolation is used in terms of wavelength. The contributions of bb and bf transitions are summed up at a given wavelength.

To perform the ray tracing efficiently, the p-PMC code was parallelized by assigning emitted photon bundles to different processors. On each processor the ray tracing was completely performed, and at the end of the simulation information about the energy per particle per processor was transmitted back to the main node. With that information, the total amount of energy absorbed per particle in the computational domain was computed on the main node. The divergence of the radiative heat flux $\nabla \cdot q$ was then

obtained from the main node by integrating the emitted energies of the radiation particles minus the total absorbed energy.

The DSMC and p-PMC coupling procedure was as follows. First, DSMC calculations were performed without considering the presence of radiation. Then, the DSMC particle information (e.g., position and F_{num}) and cell information (e.g., temperatures and number densities) were transferred to the p-PMC calculation. In this work, instead of using the particle energies, cell-averaged temperatures and number densities were used in p-PMC. The 2-D axisymmetric DSMC particle information was converted to a 3-D wedge to be used in the p-PMC method. The procedure did not require that the radial weight functions used in the DSMC and p-PMC calculations be the same. If the ratio of true to simulated particles F_{num} in a cell was different for the DSMC and p-PMC calculations, additional p-PMC particles were generated. The radiative energy change per particle due to emission and absorption was calculated by the p-PMC method. The radiative energy change in each cell $\nabla \cdot q_c$ was equally assigned to each DSMC particle as

$$\nabla \cdot q_p = \frac{\nabla \cdot q_c V_c}{N_c F_{num,c}}. \qquad (12)$$

The role of electron impact elastic and inelastic collisions of N [22] and O [23,24] has been investigated. Compared with elastic (scattering and momentum transfer) cross sections, inelastic cross sections are negligibly small for both N and O. However, due to the high collision frequency between electrons and atoms, the relaxation rates between free electrons and electronic modes are very high. Because the momentum transfer cross sections between electrons and heavy particles are on the same order as electron scattering cross sections [24], the energy exchange between free electrons and the translational mode of heavy particles occurs frequently. The energy exchange rates between free electrons and the translational and internal energies of other species in a cell by collisions are so high that the electron energy change may be assumed to be redistributed by free electrons among all the particles simultaneously during a time step. Therefore, $\nabla \cdot q_p$ is redistributed into the flowfield translational and internal energy modes assuming the equipartition among translational, rotational, and vibrational modes in this work. A new flowfield was calculated and the effect of radiation was considered in DSMC by adding $\nabla \cdot q_p \times \Delta t$ per particle at every time step. The p-PMC results of $\nabla \cdot q$ potentially remove or add energy to the DSMC flowfield. This procedure was iterated until both the flowfield and radiation were converged.

III. Numerical Flow Modeling Technique in Direct Simulation Monte Carlo

Figure 1 shows the Stardust blunt body geometry that was studied in this work, and the freestream parameters at 68.9 and 81 km altitudes are listed in Table 1. The DSMC method is implemented in the Statistical Modeling In Low-density Environment (SMILE) [25] computational tool. In this work, a single-time step average ion velocity (AIV) model [10,26] was used to model charged species in DSMC. Since charge separation is known not to be important for the conditions in this work, the efficient AIV model was selected. The computational time step is the one associated with molecular collisions rather than with the electron collision frequency, and the electron movement is determined by the average velocity of the ions per cell. In previous work [10], this model was found to maintain charge neutrality for the Stardust reentry flow conditions. The physical electron velocity (or energy) is stored per simulated electron, and this is used to calculate the collision frequency, energy exchange, and chemical reaction rates between electrons and heavy particles. In DSMC simulations, the majorant frequency scheme was employed for modeling the molecular collision frequency [27], and the VHS model was used for modeling the interaction between particles [28]. Note that in the DSMC simulations collisions are modeled between electrons and neutrals and ions but not between electrons and electrons. The viscosity index of the electron species was set to 0.1, which was shown to approximately agree with
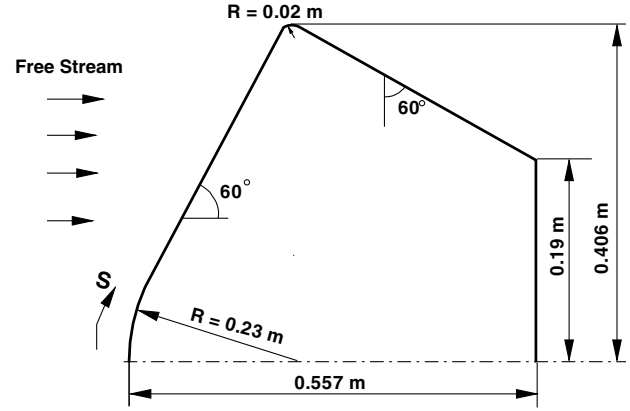

Fig. 1 Stardust geometric configuration.

electron-heavy particle collisional cross section data in Ref. [10]. Also in Ref. [10], more accurate parameters for the VHS model were obtained for $e^- + N$, $e^- + N_2$, $e^- + O$, $e^- + O_2$, and $e^- + NO$ collisions. The Borgnakke-Larsen (BL) [29] model with temperature-dependent rotational and vibrational relaxation numbers was used for modeling rotation-translation (R-T) and vibration-translation (V-T) energy transfer between neutral species, and 51 chemical reactions including 5 ionization processes were considered [17,30].

The Millikan and White (MW) [31] form of the relaxation time was used for the V-T rates, and the Parker's rates [32] for the R-T rates. At high temperatures, it is known that the vibration-rotation coupling is so strong that both vibrational and rotational collision numbers converge to a similar constant number. However, without any correction, as temperature increases (e.g., $T > 20,000$ K), the MW vibrational collision number becomes smaller than rotational collision number. Thus, in this work, a constant correction term of $\sigma_v = 1.0$ Å^2 is used to ensure that V-T collision numbers are consistent with the rotational collision numbers [33,34].

In addition, electron-vibration (e-V) relaxation was modeled using the Lee's relaxation time for N_2 [35,36]. Lee found that the maximum value of the rate coefficient for each vibrational state lies around 16,000 K [35], and that the minimum relaxation time due to the strong shape resonance effect lies around 7,000 K.

The TCE model [37] was used for modeling the chemical reactions of 11 species (N, O, N^+, O^+, N_2, O_2, NO, N_2^+, O_2^+, NO^+, and e^-). Tables 2 and 3 of Ref. [10] provide the Arrhenius rate coefficient parameters used in this work. The gas-surface interaction was modeled using the Maxwell model with total energy and momentum accommodation. The surface wall temperature varies between 500 and 2,800 K from the lee to the stagnation location, respectively, (see Ref. [12]), and full charge recombination was assumed at the wall. The time step, cell size, computational domain, and total number of simulated molecules were investigated to obtain results that are independent of these DSMC numerical parameters. At 68.9 and 81 km, approximately 3.1 and 2.7 million particles were simulated in the computational domain, respectively. The total numbers of collision (macroparameter) cells were 105,000(100,000) and 90,000 (60,000), respectively. The total number of time steps was about 100,000 with a time step of 2.0×10^{-8} and 5.0×10^{-8} s for 68.9 and 81 km altitudes, respectively. Macroparameter sampling was started

Table 1 Freestream parameters

Parameter	68.9 km	81 km
Temperature, K	224	217.6
Number density, molec/m^3	1.6028×10^{21}	2.64×10^{20}
Speed, km/s	11.9	12.4
O$_2$ mole fraction,%	23.72	23.67
N$_2$ mole fraction,%	76.28	76.23
$K_{n,\infty}$ ($L = 0.23$ m)	3.7×10^{-3}	2.3×10^{-2}

after a time step that was sufficient to reach the steady state, typically 30,000 time steps.

IV. Results and Discussion

The atomic nitrogen and oxygen radiation from Stardust reentry flowfields at 68.9 and 81 km were calculated in the DSMC and p-PMC methods. The p-PMC emission and absorption results are compared along the stagnation line with the modified NEQAIR code. The NEQAIR code was modified to calculate E_{emis}, E_{abs}, and $\nabla \cdot q$ for each cell in the tangent-slab approximation [16]. In the p-PMC method, $E_{\mathrm{emis},p}$, $E_{\mathrm{abs},p}$, and $\nabla \cdot q_p$ are calculated per particle, and to compare with NEQAIR, the particle energies are averaged in each cell by the following equation

$$E_c[\mathrm{W/cm^3}] = \sum_{k=1}^{N_c} E_{p,k}[\mathrm{W}]/F_{\mathrm{num}} \times n_a/N_c \qquad (13)$$

where n_a is the number density of the atomic species in the cell, and N_c is the number of particles in the cell.

There is no unique way to select the number of photon ray bundles, the size of the cone ray, or the number of p-PMC particles per cell, and the ultimate selection of these parameters comes from a number of considerations. These issues were investigated in Ref. [16] and are summarized here. For homogeneous gas cases, the p-PMC results were compared with theoretical values, and it was found that more particles result in more intersections for each ray, and the increase in the number of intersections per ray reduced the deviation from the theoretical solution. When the deviation was high, some rays were incorrectly escaping from the high-emission region without being absorbed by particles, resulting in an incorrect, lower-absorption prediction. As the number of particles increases (i.e., a simulated particle represents less real atoms), the contribution of a specific particle to the optical thickness represented by a simulated particle $\Delta\tau$ decreases. Therefore, it was found to be important to have a sufficient number of intersections per ray especially in the high-optically thickness gradient regions. In addition, two test cases of a homogeneous 100% atomic oxygen slab of gas and a 100% O in a 5 km/s speed shock were performed to validate the selection of the final p-PMC numerical parameters and the accuracy of the random number databases. This was particularly important since this is the first application of the p-PMC method to a high-gradient shock and a rarefied-gas condition. For the 5 km/s 100% O bow-shock flowfields, a tangent-slab, 1-D disk flowfield was created using the flowfield information along the stagnation streamline to compare directly with the tangent-slab NEQAIR results. For both the gray and nongray uniform flowfield and the 5 km/s shock cases, good agreement between the p-PMC and tangent-slab NEQAIR results for E_{emis} and E_{abs} was obtained along the stagnation line. The p-PMC numerical parameters obtained from the aforementioned tests, were used to obtain the results to be discussed in Subsections IV.B and IV.C below.

A. Stardust Flowfield at 68.9 and 81 Kilometers Without Radiation

Figures 2 and 3 show contour plots of the electron number density and electron temperature for the Stardust blunt body at the two altitudes of 68.9 and 81 km, respectively. It may be seen that the shock standoff distance increases as the altitude becomes higher because the shock is weaker. At 68.9 km, the flow is more continuumlike, and there is a sufficient number of collisions that results in thermal excitation and ionization reactions in the stagnation region. Because of the strong shock, most molecules are dissociated in the region. Therefore, the rotational and vibrational temperatures off the stagnation line were represented by the molecular particles that entered off the stagnation region. That is, the peak of temperatures were found to be in the stagnation region at this altitude. On the other hand, at 81 km, the maximum total number density and electron number density are observed at the shoulder of the Stardust body. The maximum electron temperature is also observed at the shoulder of the body, and thus the maximum emission may be off the
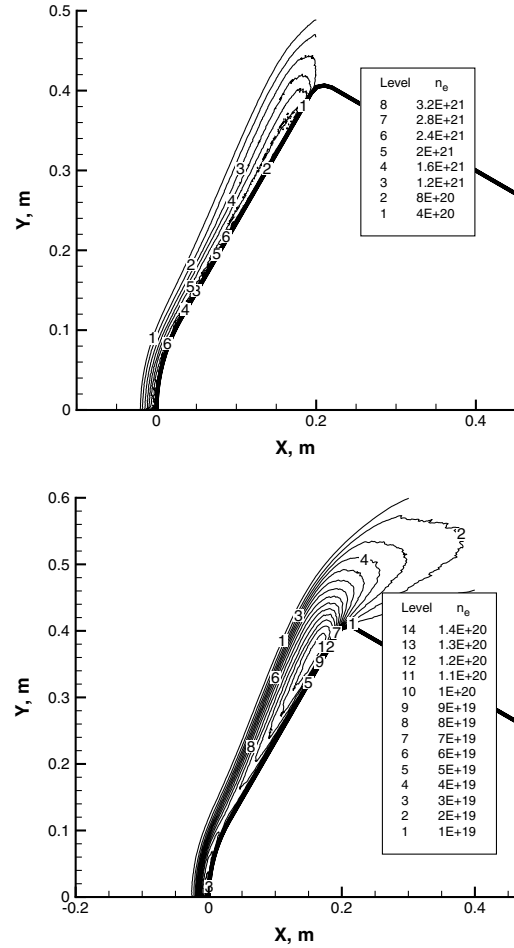

Fig. 2 Contours of the electron number density for the Stardust blunt body at 68.9 km (top) and 81 km (bottom) altitudes.

stagnation point. The majority of the gas particles pass through a strong shock wave, and flow around the body without being cooled by collisions with the surface. The shock is not too strong at this altitude, and thus molecular particles remain in the stagnation region. Since these particles travel a greater distance through the shock layer than those particles that flow along the stagnation streamline, they experience a greater number of collisions that result in thermal excitation and chemical reactions. The peak of both rotational and vibration temperature occurs off the stagnation line, and the e-V energy exchange is so efficient that the peak of electron temperature can be found off the stagnation line. The higher electron number density is attributed to the higher electron temperature and higher ionization rates. Because of the nonequilibrium nature of the flow, the peak number of reactions can occur off of the stagnation streamline but on the shoulder of the body at 81 km. Note that in the modeling of the flow around the blunt body shape of the Aeroassist Flight Experiment [38,39] a similar feature was observed. This is one of the thermochemical nonequilibrium influences. The maximum degree of ionization is approximately 7% and 3% at 68.9 and 81 km, respectively, and the maximum electron temperature is about 20,000 K and 16,000 K at 68.9 and 81 km, respectively.

Figure 4 shows distributions of total, ion, and electron number densities along the stagnation line for the Stardust blunt body at the two altitudes. As shown in the figure, the density gradient at 68.9 km is much higher than the 1 at.81 km. Both ions and electrons are produced within $x = -0.03$ m at both altitudes, and the charge neutrality implementation scheme is validated in the shock region. Figure 5 shows distributions of N, O, $\mathrm{N^+}$, $\mathrm{O^+}$, NO, and $\mathrm{N_2^+}$ number densities along the stagnation line. For both cases the dissociation rate is so high that atomic N and O species dominate. At the lower altitude, the higher ionization rate is consistent with the presence of the $\mathrm{N^+}$ ionic species.
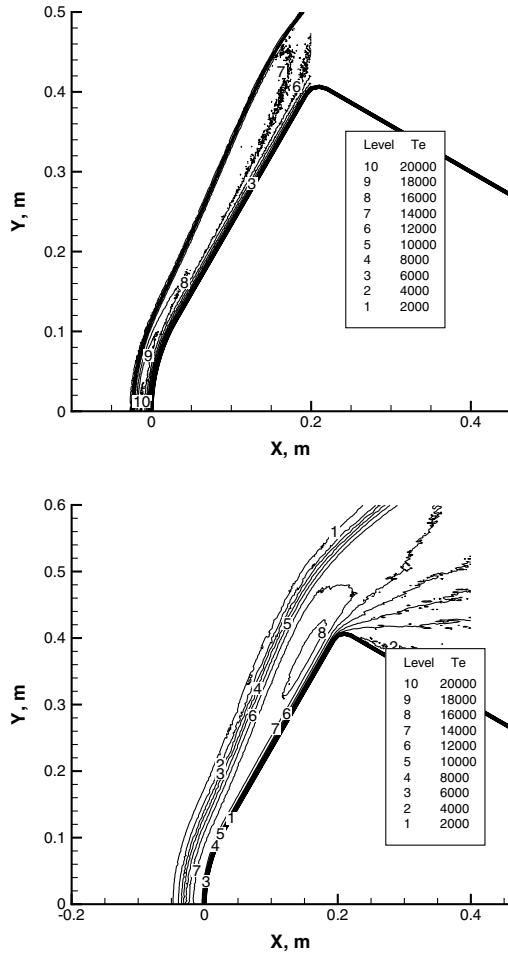
Fig. 3 Contours of the electron temperature for the Stardust blunt body at 68.9 km (top) and 81 km (bottom) altitudes.
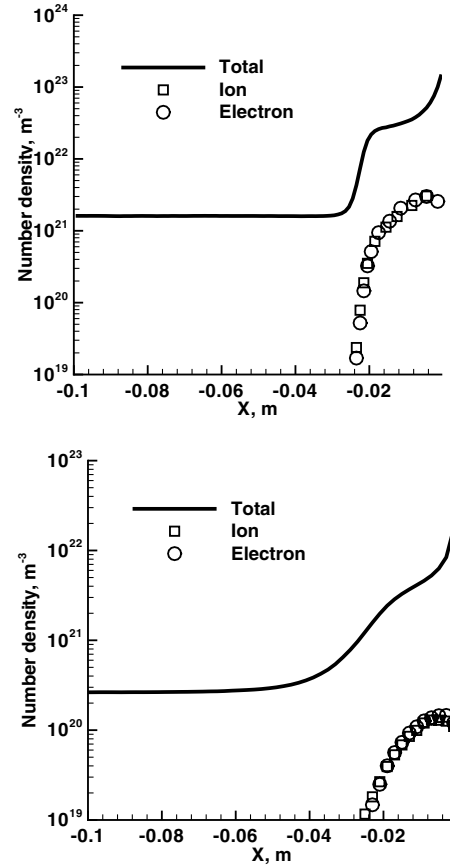

Fig. 4 Distributions of total, ion, and electron number densities along the stagnation line for the Stardust blunt body at 68.9 km (top) and 81 km (bottom) altitudes.

Distributions of translational, rotational, vibrational, and electron temperatures along the stagnation line are shown in Fig. 6. Although the maximum translational temperature is as high as 60,000 K, the internal and electron temperatures are lower than 20,000 K. The maximum electron temperature is as high as 20,000 K at 68.9 km and 16,000 K at 81 km in the stagnation region. At 68.9 km, the overshoot phenomenon can be seen between $x = -0.03$ and -0.02 m, and the difference between translational and other temperatures is less than 10,000 K between $x = -0.02$ and 0 m. The flow at 81 km exhibits a higher degree of thermal nonequilibrium. Note that although electronic excited states are not modeled in this work, the consideration of electronic modes is estimated not to impact the flowfield significantly because fractions of electronically excited states are small.

Using the DSMC Stardust flowfield and the database of Sohn et al. [20], the emission energies of N, O, N_2^+, N_2, O_2, and NO species along the stagnation line for the Stardust blunt body at 68.9 and 81 km altitudes were calculated and are presented in Fig. 7. It may be seen that for these flow conditions the molecular radiation is more than 2 orders of magnitude lower than N radiation inside the shock, and NO radiation cannot be seen in the figure because the emission energy is too low. Far from the body, the magnitude of radiation between atoms and molecules is approximately the same, but the magnitude is too low to impact the flowfield gas dynamics. Therefore, in this work, we focus on the atomic N and O radiation sources.

B. Atomic Oxygen Radiation at 81 Kilometers

First, atomic oxygen radiation was calculated by the p-PMC method and compared with NEQAIR. Atomic oxygen was used as a test species because its number of bound–bound transition lines are about half of atomic N. In this work, the p-PMC method is applied

for high-gradient, nonequilibrium, rarefied-gas conditions for the first time. Thus, using the stagnation line flowfield information at 81 km, a tangent-slab, 1-D disk Stardust flowfield was created to validate the p-PMC calculations by comparing with the tangent-slab NEQAIR results. Figure 8 shows comparisons of O emission and absorption energies between p-PMC and NEQAIR for the tangent-slab, 1-D disk Stardust flowfield at 81 km along the stagnation line. The interpolated emission using the database over the high-gradient number density and temperature shock profile was found to agree well with the NEQAIR results. It is also shown that with regard to the O absorption (i.e., radiative energy change $\nabla \cdot q$), good agreement is obtained between p-PMC and NEQAIR for the tangent-slab, 1-D disk case. Secondly, the p-PMC calculations were performed for the 2-D axisymmetric Stardust flowfield at 81 km. Figure 9 shows comparisons of O emission and absorption energies between p-PMC and NEQAIR along the stagnation line. In the comparison, the p-PMC results are averaged over cells of $\Delta y = 1$ cm to reduce the statistical noise since the flowfield is approximately the same in the stagnation region and Δx is the same as the DSMC cell size. The ratio of shock thickness to the Stardust blunt body radius is smaller than $1/10$ in the stagnation region. Therefore, it is reasonable that p-PMC results are similar to the tangent-slab case.

C. Atomic Nitrogen and Atomic Oxygen Radiation at 68.9 and 81 Kilometers

In this subsection, the p-PMC method was performed for gas mixture cases. Atomic N and O radiation energies were calculated by the p-PMC method using the 2-D axisymmetric Stardust flowfield at 68.9 and 81 km. As mentioned earlier, the difference between translational and electron temperatures is higher than 40,000 K in the shock at 81 km, and thus the high-nonequilibrium effects are important for both altitudes. At 81 km, F_{num} is set to 2.5×10^{10}, a radial weight function was used with a spatial resolution $\Delta y = 2$ cm,
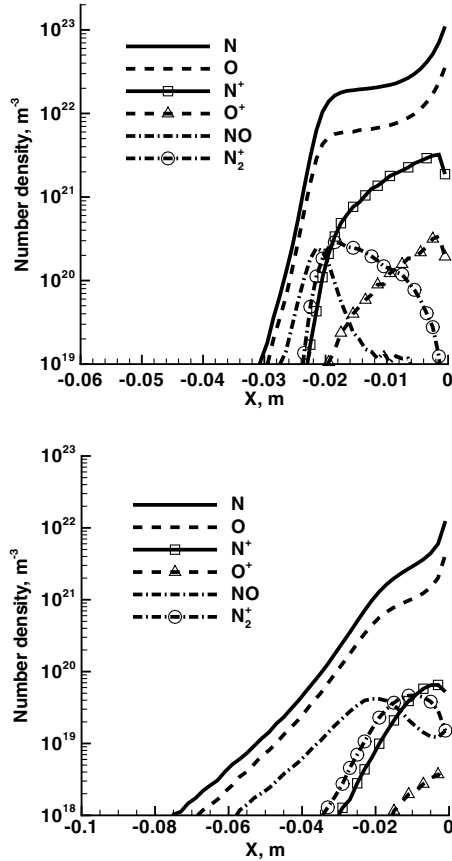
Fig. 5   Distributions of N, O, N$^+$, O$^+$, NO, and N$_2^+$ number densities along the stagnation line for the Stardust blunt body at 68.9 km (top) and 81 km (bottom) altitudes.
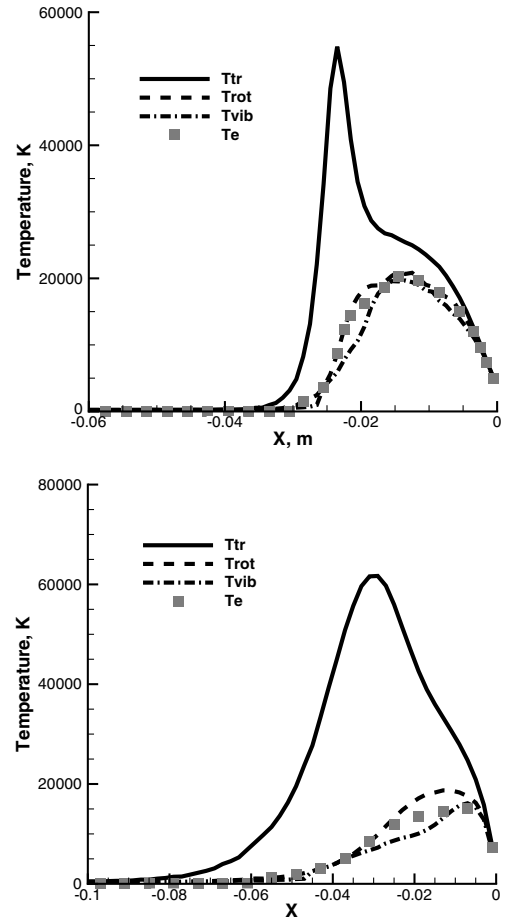

Fig. 6   Distributions of the translational, rotational, and vibrational temperatures, and electron temperature along the stagnation line for the Stardust blunt body at 68.9 km (top) and 81 km (bottom) altitudes.

and the cone angle was set to 2 deg. The number of rays was 10 million and the p-PMC calculations were iterated five times to reduce the statistical error. Similar to the previous subsection, good agreement was obtained for both the N and O emission and absorption energies at 81 km. The maximum of the N emission is $4,000$ W/cm^3 at this altitude, which is approximately 1 order of magnitude higher than O emission because of the higher concentration of N and N$^+$ than O and O$^+$ in the shock. (See Fig. 9 for the O radiation, and see Fig. 17 of Ref. [16] for the N radiation.) It was also found that correlations between N and O are not significant because the important atomic lines for each species do not overlap each other.

At 68.9 km, comparisons of the N and O emission and $\nabla \cdot q$ energies between p-PMC and NEQAIR for the 2-D axisymmetric Stardust flowfield along the stagnation line are shown in Figs. 10 and 11, respectively. Note that the flowfield condition is optically so thick that the magnitude of emission and absorption energies for N and O are approximately the same. For this altitude, $F_{num} = 1 \times 10^{11}$ and a radial weight function were used with $\Delta y = 2.5$ cm. Similar to the 81 km case, the cone angle and the number of rays were set to 2 deg and 10×10^6, respectively, and the p-PMC calculations were iterated five times to reduce the statistical error. As shown in the figures, the magnitude of emission and $\nabla \cdot q$ agreed well between the p-PMC and NEQAIR tangent-slab solutions. Note that since the p-PMC results are averaged over several cells in the radial direction between 0 and 1 cm, the p-PMC results are slightly different from the NEQAIR, especially in the region between $x = -1.2$ and -0.8 cm.

Finally, in Figs. 12 and 13, contours of the N emission energy in W/cm^3 calculated by the p-PMC method are shown for the Stardust blunt body at 68.9 km and 81 km altitudes, respectively. It was found that although the radiation peak is in the stagnation region at 68.9 km, the radiation peak is on the shoulder of the body at 81 km. At 68.9 km, the flow is near continuum, and there are a sufficient number of collisions that results in thermal excitation and ionization reactions

in the stagnation region. The maximum emission energy is approximately 85,000 and 4,000 W/cm^3 at 68.9 and 81 km altitudes, respectively.

D.   Stardust Flowfield at 68.9 Kilometers with Atomic Radiation

The effect of energy change on the flowfield due to atomic radiation was investigated at both 68.9 and 81 km altitudes in the DSMC for the first time, to the best of our knowledge. At 81 km altitude, since the intensity of radiation energy is not high, it was found that the radiation did not change the flowfield. However, energy change due to radiation is more important for denser flows, and calculations were performed at 68.9 km altitude. Subsequent p-PMC 68.9 km case calculations and loosely coupled DSMC calculations were iterated eight times. To reduce the radiation energy noise due to the electron temperature deviation in the flowfield and absorption energy deviation error in the ray-tracing, the radiation energy change $\nabla \cdot q$ was smoothed.

To investigate the effect of atomic radiation three cases, 1) without radiation, 2) first iteration with $\nabla \cdot q$, and 3) final iteration with $\nabla \cdot q$, are compared. Figure 14 shows a comparison of the distributions of the N number densities along the stagnation line on a linear scale among these three cases. Figure 15 presents distributions of the rotational, vibrational, and electron temperatures along the stagnation line for case 2, and a comparison of the distribution of translational temperature between cases 1 and 2. Although the maximum translational temperature is as high as 55,000 K, other temperatures are lower than 20,000 K as shown in Figs. 6 (top) and 15. In the figures, the overshoot phenomenon can be seen to be between $x = -0.03$ and -0.02 m, and the difference between the translational and other temperatures is less than 10,000 K between $x = -0.02$ and 0 m.
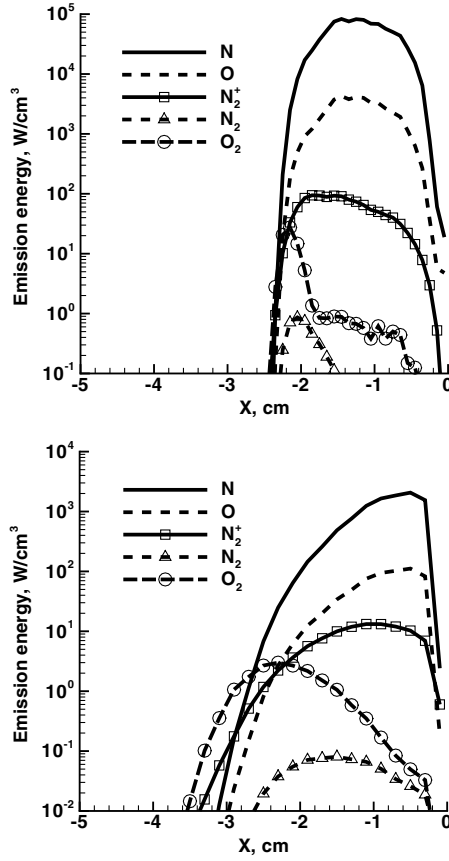
Fig. 7 Distributions of N, O, N_2^+, N_2, O_2, and NO emission energies along the stagnation line for the Stardust blunt body at 68.9 km (top) and 81 km (bottom) altitudes.
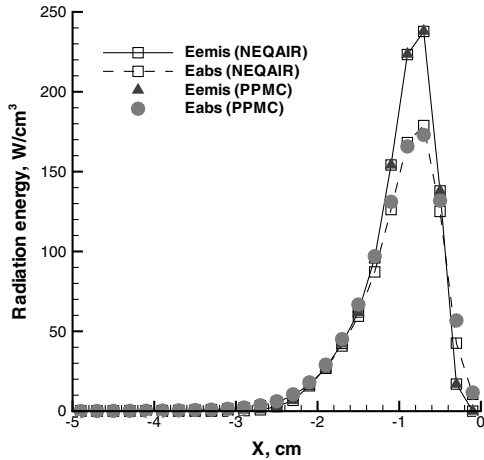

Fig. 8 Comparisons of O emission and absorption energies between NEQAIR and p-PMC for the tangent-slab, 1-D disk Stardust flowfield at 81 km along the stagnation line.

Fig. 9 Comparisons of O emission and absorption energies between NEQAIR and p-PMC for the Stardust flowfield at 81 km along the stagnation line.

Fig. 10 Comparison of the emission energy between p-PMC and NEQAIR for the Stardust flowfield at 68.9 km along the stagnation line.

Fig. 11 Comparison of the $\nabla \cdot q$ energy between p-PMC and NEQAIR for the Stardust flowfield at 68.9 km along the stagnation line.

The radiation energy slightly affects the chemistry in the flowfield. As shown in Fig. 14, the N number densities are slightly higher than the case without radiation, and the gradient of concentration is slightly lower near the body. Because of the decrease of temperatures between $x = 0$ and -0.015 m, the pressure is lower in this region, resulting in the diffusion of particles upstream. It was also found that when the radiative energy was removed from the flow the O^+ number density slightly increased inside the shock due to the increase of the O number density. On the other hand, the N_2^+ number density was decreased slightly near $x = -0.013$ m because the lower translational temperature reduces the ionization rate for $N + N \rightarrow$
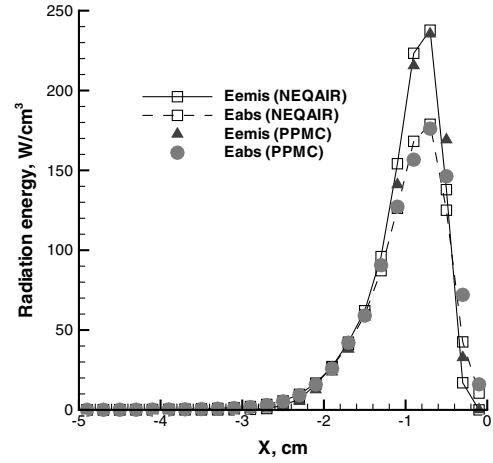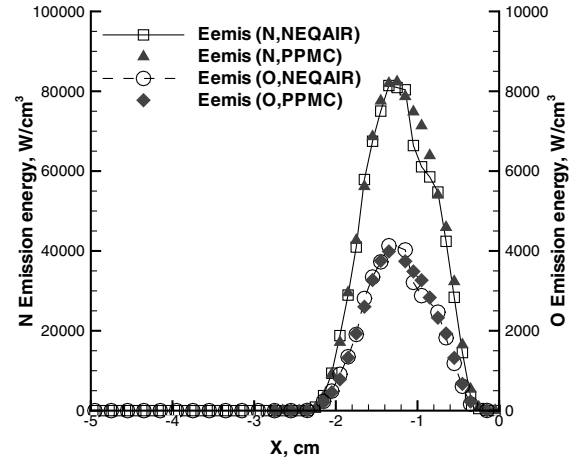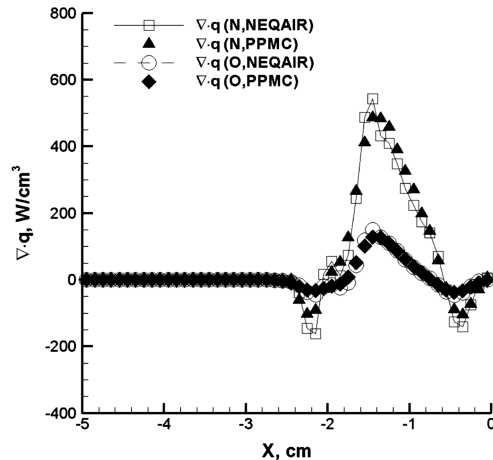
$e^- + N_2^+$. The high-electron temperature region becomes smaller and moves slightly in the upstream direction because the atomic radiation energy loss near the body lowers the gas temperatures. Along the stagnation line the temperatures are decreased between $x = 0$ and -0.015 m near the body due to radiation energy loss, as
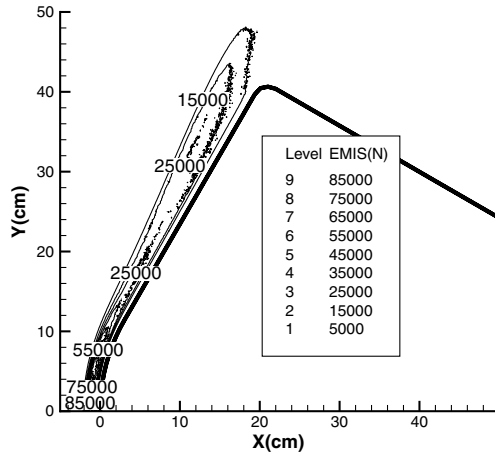
Fig. 12   Contours of the N emission energy in W/cm³ calculated by *p*-PMC for the Stardust blunt body at 68.9 km.
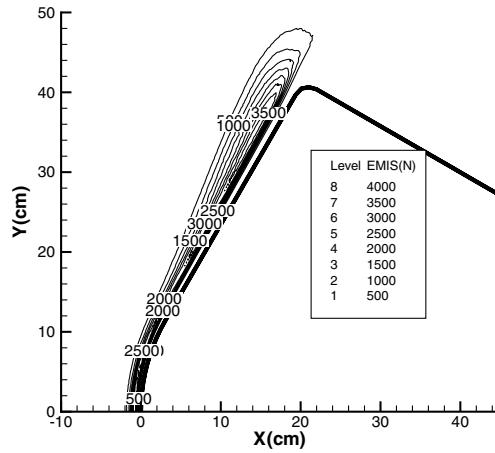

Fig. 13   Contours of the N emission energy in W/cm³ calculated by *p*-PMC for the Stardust blunt body at 81 km.
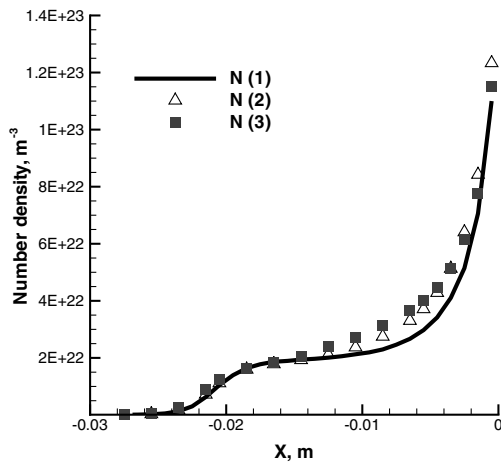

Fig. 14   Comparison of distributions of N number densities on a linear scale among cases: 1) without radiation, 2) first iteration with $\nabla \cdot q$ coupling, and 3) final iteration with $\nabla \cdot q$ coupling, for the Stardust body at 68.9 km along the stagnation line.
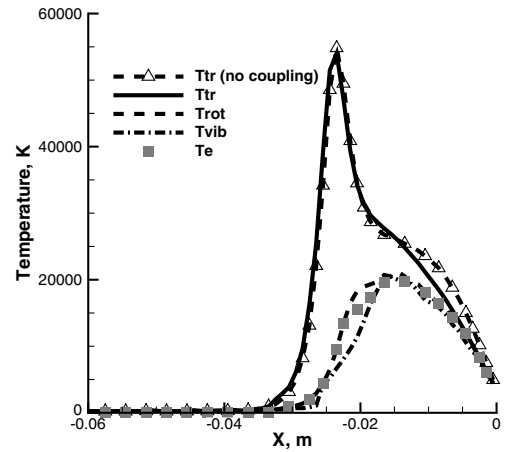

Fig. 15   A comparison of distributions of the translational temperature between the no radiation coupling case 1, and the first iteration with $\nabla \cdot q$ coupling case 2, and distributions of the rotational, vibrational, and electron temperatures for case 2 for the Stardust body at 68.9 km along the stagnation line.
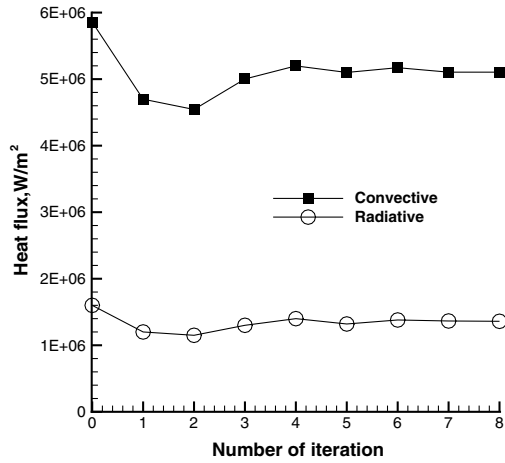

Fig. 16   Convective and radiative heat fluxes at the stagnation point at each iteration between DSMC and *p*-PMC coupling for the Stardust body at 68.9 km.

compared Fig. 15 with Fig. 6. The translational temperature is decreased by approximately 5,000 K and other temperatures are decreased by approximately 1,000–3,000 K. Between cases 2 and 3 significant differences in temperatures were not observed. Compared with the first iteration case 2, the temperatures are slightly increased

near the wall in the converged solution 3 because of the lower emission than the first iteration case.

The heat flux to the wall was calculated and compared between the cases with and without radiation. In Fig. 16 the convective and radiative heat fluxes at the stagnation point are shown at each iteration between DSMC and *p*-PMC. The convective and radiative heat fluxes at the stagnation point were approximately 5.9×10^6 and 1.6×10^6 W/m² without radiation, respectively. At this altitude, the radiative flux on the stagnation point was found to be approximately 27% of convective heat flux. As the number of iterations with the *p*-PMC radiation increases, the heat flux at the stagnation converged to approximately 5.2×10^6 W/m². For the first few iterations, due to the high temperature, radiation was overestimated and resulted in lower convective heat flux on the wall. With radiation coupling, the lower temperature and lower gradient near the body resulted in lower convective heat flux to the wall. The inclusion of radiation changes the convective heat flux by approximately 12%, and the radiative heat flux to the wall was also decreased by approximately 15%.

V.   Conclusions

The Stardust reentry flows were simulated at near continuum and transitional altitudes using the DSMC method. Atomic radiation energies were calculated by the *p*-PMC method, and we succeeded in loosely coupling the DSMC with the *p*-PMC method for the first time. Eleven species, including five ionization processes, were

modeled in DSMC, and the average ion velocity model was used for electron movement. The degree of ionization was predicted to be 7 and 3% along the stagnation line at 68.9 and 81 km, respectively. While the translational temperature is as high as 60,000 K, the maximum electron temperature is approximately 20,000 K at 68.9 km. To capture this high-nonequilibrium effect, the NEQAIR-based absorption cross section databases for N and O were used, and the p-PMC calculations were performed for N and O radiation using the efficient random number databases for emission and wavelength selection calculations. The molecular radiation was not considered in this work because the contribution of molecules to radiation is less than 1%.

It was found that the N emission is approximately 1 order of magnitude higher than the O emission along the stagnation line. Along the stagnation line, the p-PMC results agreed well with the tangent-slab NEQAIR results because the shock is so thin that the shock curvature does not influence the stagnation region. In the p-PMC method, the maximum radiation energy was found to be on the shoulder of the body at 81 km where the electron temperature is the maximum; however, the maximum radiation energy was found to be in the stagnation region at 68.9 km. When the energy change due to radiation was taken into account in the DSMC calculations, the coupling resulted in lower temperatures inside the shock and a reduction in the convective heat flux to the body in the stagnation region by approximately 12% at 68.9 km. At 68.9 km, the radiative heat flux in the stagnation region on the surface was calculated by the p-PMC method and it is approximately 25% of convective heat flux. However, at 81 km altitude the atomic radiation does not impact the flowfield significantly.

Acknowledgments

References

[1] Olynick, D., Chen, Y.-K., and Tauber, M. E., "Aerothermodynamics of the Stardust Sample Return Capsule," *Journal of Spacecraft and Rockets*, Vol. 36, No. 3, 1999, pp. 442–462.
doi:10.2514/2.3466

[2] Park, C., "Calculations of Stagnation-Point Heating Rates Associated with Stardust Vehicle," AIAA Paper 2005-190, Jan. 2005.

[3] Boyd, I. D., Trumble, K., and Wright, M. J., "Nonequilibrium Particle and Continuum Analyses of Stardust Entry for Near-Continuum Conditions," AIAA Paper 2007-4543, June 2007.

[4] Johnston, C. O., Gnoffo, P. A., and Sutton, K., "Influence of Ablation on Radiative Heating for the Earth Entry," *Journal of Spacecraft and Rockets*, Vol. 46, No. 3, 2009, pp. 481–491.
doi:10.2514/1.40290

[5] Prabhu, D., Saunders, D., Liu, Y., Hash, D., and Dateo, C., "Preliminary Estimates of Radiative Heating for the CEV Heatshield," NASA CAP TN/EG-CEV-06-8, Jan. 2006.

[6] Kinney, D. J., "Development of the ORION Crew Exploration Vehicle's Aerothermal Database Using a Combination of High Fidelity CFD and Engineering Level Methods," AIAA Paper 2009-1100, NASA Ames Research Center, Jan. 2009.

[7] Johnson, E. J., Starkey, R. P., and Lewis, M. J., "Aerodynamic Stability of Reentry Heat Shield Shapes for a Crew Exploration Vehicle," *Journal of Spacecraft and Rockets*, Vol. 43, No. 4, 2006, pp. 721–730.
doi:10.2514/1.20044

[8] Bose, D., McCorkle, E. M., Thompson, C., Bogdanoff, D., Prabhu, D. K., and Allen, G. A., "Analysis and Model Validation of Shock Layer Radiation in Air," AIAA Paper 2008-1246, Jan. 2008.

[9] Johnston, C. O., Gnoffo, P., and Mazaheri, A., "A Study of Ablation-Flowfield Coupling Relevant to Orion HeatShield," AIAA Paper 2009-4318, June 2009.

[10] Ozawa, T., Zhong, J., and Levin, D. A., "Development of Kinetic-based Energy Exchange Models For Non-Continuum, Ionized Hypersonic Flows," *Physics of Fluids*, Vol. 20, No. 4, 2008, p. 046102.
doi:10.1063/1.2907198.

[11] Gnoffo, P. A., Johnston, C. O., and Thompson, R. A., "Implementation of Radiation, Ablation, and Free Energy minimization Modules for Coupled Simulations of Hypersonic Flow," AIAA Paper 2009-1399, Jan. 2009.

[12] Zhong, J., Ozawa, T., and Levin, D. A., "Modeling of Stardust Reentry Ablation Flows in the Near-Continuum Flight Regime," *AIAA Journal*, Vol. 46, No. 10, Oct. 2008, pp. 2568–2581.
doi:10.2514/1.36196

[13] Gallis, M. A., and Harvey, J. K., "Nonequilibrium Thermal Radiation from Air Shock Layers Modeled with Direct Simulation Monte Carlo," *Journal of Thermophysics and Heat Transfer*, Vol. 8, No. 4, 1994, pp. 765–772.
doi:10.2514/3.610

[14] Gallis, M. A., and Harvey, J. K., "Atomic Species Radiation from Air Modeled with Direct Simulation Monte Carlo Method," *Journal of Thermophysics and Heat Transfer*, Vol. 9, No. 3, 1995, pp. 456–463.
doi:10.2514/3.687

[15] Wang, A., and Modest, M. F., "Photon Monte Carlo Simulation for Radiative Transfer in Gaseous Media Represented by Discrete Particle Fields," *Journal of Heat Transfer*, Vol. 128, No. 10, 2006, pp. 1041–1049.
doi:10.1115/1.2345431.

[16] Ozawa, T., Wang, A., Modest, M., and Levin, D. A., "Development of a Coupled DSMC—Particle Photon Monte Carlo Method for Simulating Atomic Radiation in Hypersonic Reentry Flows," Seattle, Washington, AIAA Paper 2008-3916, June 2008.

[17] Park, C., *Nonequilibrium Hypersonic Aerothermodynamics*, Wiley, New York, 1990.

[18] Modest, M. F., *Radiative Heat Transfer*, Academic Press, New York, 2003.

[19] Whiting, E. E., Park, C., Liu, Y., Arnold, J. O., and Paterson, J. A., "NEQAIR 96, Nonequilibrium and Equilibrium Radiative Transport and Spectra Program: User's Manual," NASA RP-1389, 1996.

[20] Sohn, I., Bansal, A., Levin, D. A., and Modest, M., "Advanced Radiation Calculations of Hypersonic Reentry Flows Using Efficient Databasing Schemes," AIAA Paper 2008-4091, June 2008.

[21] Ozawa, T., Modest, M. F., and Levin, D. A., "Spectral Module for Photon Monte Carlo Calculations in Hypersonic Nonequilibrium Radiation," *ASME Journal of Heat Transfer*, Vol. 132, No. 2, 2010, (accepted).

[22] Thomas, L. D., and Nesbet, R. K., "Low Energy Electron Scattering by Atomic Nitrogen," *Physical Review A*, Vol. 12, No. 6, 1975, pp. 2369–2377.
doi:10.1103/PhysRevA.12.2369

[23] Blaha, M., and Davis, J., "Elastic Scattering of Electrons by Oxygen and Nitrogen at Intermediate Energies," *Physical Review A*, Vol. 12, No. 6, 1975, pp. 2319–2324.
doi:10.1103/PhysRevA.12.2319

[24] Itikawa, Y., and Ichimura, A., "Cross Sections for Collisions of Electrons and Photons with Atomic Oxygen," *Journal of Physical and Chemical Reference Data*, Vol. 19, No. 3, 1990, pp. 637–651.

[25] Ivanov, M. S., Markelov, G. N., and Gimelshein, S. F., "Statistical Simulation of Reactive Rarefied Flows: Numerical Approach and Applications," AIAA Paper 1998-2669, June 15–18 1998.

[26] Boyd, I. D., "Monte Carlo Simulation of Nonequilibrium Flow in a Low-Power Hydrogen Arcjet," *Physics of Fluids*, Vol. 9, No. 10, 1997, pp. 3086–3095.
doi:10.1063/1.869474.

[27] Ivanov, M. S., and Rogasinsky, S. V., "Analysis of the Numerical Techniques of the Direct Simulation Monte Carlo Method in the Rarefied Gas Dynamics," *Soviet Journal of Numerical Analysis and Mathematical Modeling*, Vol. 3, No. 6, 1988, pp. 453–465.
doi:10.1515/rnam.1988.3.6.453.

[28] Bird, G. A., "Monte-Carlo Simulation in an Engineering Context," *Rarefied Gas Dynamics*, edited by S. Fisher, Vol. 74, AIAA, New York, 1981, pp. 239–255.

[29] Borgnakke, C., and Larsen, P. S., "Statistical Collision Model for Monte Carlo Simulation of Polyatomic Gas Mixture," *Journal of Computational Physics*, Vol. 18, No. 4, 1975, pp. 405–420.
doi:10.1016/0021-9991(75)90094-7

[30] Bird, G. A., "Nonequilibrium Radiation During Re-Entry at 10 km/s," AIAA Paper 87-1543, June 1987.

[31] Millikan, R. C., and White, D. R., "Systematics of Vibrational Relaxation," *Journal of Chemical Physics*, Vol. 39, No. 12, 1963, pp. 3209–3213.
doi:10.1063/1.1734182

[32] Parker, J. G., "Rotational and Vibrational Relaxation in Diatomic Gases," *Physics of Fluids*, Vol. 2, No. 4, 1959, pp. 449–462.
doi:10.1063/1.1724417.

[33] Park, C., "Problems of Rate Chemistry in the Flight Regimes of Aeroassisted Orbital Transfer Vehicles," *Thermal Design of Aeroasisted Orbital Transfer Vehicles*, edited by H. F. Nelson, Vol. 96, AIAA, New York, 1985, pp. 511–537.

[34] Park, C., "Assessment of Two-Temperature Kinetic Model for Ionizing Air," *Journal of Thermophysics and Heat Transfer*, Vol. 3, No. 3, 1989, pp. 233–244.
doi:10.2514/3.28771

[35] Lee, J. H., "Electron-Impact Vibrational Excitation Rates in the Flowfield of Aeroassisted Orbital Transfer Vehicles," *Thermophysical Aspects of Reentry Flows*, edited by J. N. Moss, and C. D. Scott, Vol. 103, AIAA, New York, 1986, pp. 197–224.

[36] Lee, J. H., "Electron-Impact Vibrational Relaxation in High-Temperature Nitrogen," *Journal of Thermophysics and Heat Transfer*, Vol. 7, No. 3, Sept. 1993, pp. 399–405.
doi:10.2514/3.432

[37] Bird, G. A., "Simulation of Multi-Dimensional and Chemically Reacting Flows," *Rarefied Gas Dynamics*, edited by R. Campargue, AIAA, New York, 1979, pp. 365–388.

[38] Candler, G., and Park, C., "The Computation of Radiation from Nonequilibrium Hypersonic Flows," AIAA Paper 1988-2678, June 1988.

[39] Candler, G. V., "The Computation of Weakly Ionized Hypersonic Flows in Thermo-Chemical Nonequilibrium," Ph.D. Thesis, Stanford Univ., Stanford, CA, 1988.